




Article

New Insight into Assembled Fe₃O₄@PEI@Ag Structure as Acceptable Agent with Enzymatic and Photothermal Properties

Teng Wang^{1,2,†}, Xi Hu^{1,2,†}, Yujun Yang³, Qing Wu^{1,2}, Chengdian He^{1,2}, Xiong He^{1,2}, Zhenyu Wang^{1,2,*} and Xiang Mao^{1,2,*} 

¹ State Key Laboratory of Ultrasound in Medicine and Engineering, College of Biomedical Engineering, Chongqing Medical University, Chongqing 400016, China

² Chongqing Key Laboratory of Biomedical Engineering, Chongqing Medical University, Chongqing 400016, China

³ Key Laboratory of Laboratory Medical Diagnostics, Ministry of Education, Department of Laboratory Medicine, Chongqing Medical Laboratory Microfluidics and SPRi Engineering Research Center, Chongqing Medical University, Chongqing 400016, China

* Correspondence: 203853@cqmu.edu.cn (Z.W.); maox@cqmu.edu.cn (X.M.)

† These authors contributed equally to this work.

Abstract: Metal-based enzyme mimics are considered to be acceptable agents in terms of their biomedical and biological properties; among them, iron oxides (Fe₃O₄) are treated as basement in fabricating heterogeneous composites through variable valency integrations. In this work, we have established a facile approach for constructing Fe₃O₄@Ag composite through assembling Fe₃O₄ and Ag together via polyethyleneimine ethylenediamine (PEI) linkages. The obtained Fe₃O₄@PEI@Ag structure conveys several hundred nanometers (~150 nm). The absorption peak at 652 nm is utilized for confirming the peroxidase-like activity of Fe₃O₄@PEI@Ag structure by catalyzing 3,3',5,5'-tetramethylbenzidine (TMB) in the presence of H₂O₂. The Michaelis–Menten parameters (K_m) of 1.192 mM and 0.302 mM show the higher catalytic activity and strong affinity toward H₂O₂ and TMB, respectively. The maximum velocity (V_{max}) value of 1.299 × 10⁻⁷ M·s⁻¹ and 1.163 × 10⁻⁷ M·s⁻¹ confirm the efficiency of Fe₃O₄@PEI@Ag structure. The biocompatibility illustrates almost 100% cell viability. Being treated as one simple colorimetric sensor, it shows relative selectivity and sensitivity toward the detection of glucose based on glucose oxidase. By using indocyanine green (ICG) molecule as an additional factor, a remarkable temperature elevation is observed in Fe₃O₄@PEI@Ag@ICG with increments of 21.6 °C, and the absorption peak is nearby 870 nm. This implies that the multifunctional Fe₃O₄@PEI@Ag structure could be an alternative substrate for formatting acceptable agents in biomedicine and biotechnology with enzymatic and photothermal properties.

Keywords: Fe₃O₄@PEI@Ag; assembling process; enzymatic; catalytic performance; photothermal property



Citation: Wang, T.; Hu, X.; Yang, Y.; Wu, Q.; He, C.; He, X.; Wang, Z.; Mao, X. New Insight into Assembled Fe₃O₄@PEI@Ag Structure as Acceptable Agent with Enzymatic and Photothermal Properties. *Int. J. Mol. Sci.* **2022**, *23*, 10743. <https://doi.org/10.3390/ijms231810743>

Academic Editors: Andrea Salis and Christian M. Julien

Received: 23 June 2022

Accepted: 11 August 2022

Published: 15 September 2022

Publisher's Note: MDPI stays neutral with regard to jurisdictional claims in published maps and institutional affiliations.



Copyright: © 2022 by the authors. Licensee MDPI, Basel, Switzerland. This article is an open access article distributed under the terms and conditions of the Creative Commons Attribution (CC BY) license (<https://creativecommons.org/licenses/by/4.0/>).

1. Introduction

Transition metal-based functional materials exhibit unique properties that could be ascribed to their structural electronic status or elemental integrations [1–4]. Particularly, they demonstrate high quality and use in various applications according to different requirements in oxide or dioxide compositions [5,6]. Conventionally, they convey particular characterization because of the d-electrons effect in full utilizations. It is worth noting that iron oxide nanoparticles (Fe₃O₄ NPs) are fundamental transition oxides, with expected applications as magnetic, biocompatible, and nontoxic agents [7,8]. In applied strategies, Fe₃O₄ NPs possess intrinsic reaction activities because of their metal bond capacity and variable valency [9]. In previous works, the characteristics of Fe₃O₄ NPs have mainly been investigated in enzymatic performances at initial times [10]. These pioneering works improved the possibility that Fe₃O₄ materials could integrate other functional agents as novel types of enzyme mimics. In these comparisons, Fe₃O₄ series enzyme mimics showed

high stability and efficiency in catalytic performances, the same as natural enzymes exhibit under harsh reaction conditions [9–11]. Moreover, they reflected that Fe_3O_4 NPs have potential capacity and were considered as a competitive agent in forming heterogeneous fabrications. Additionally, the regular requirements for the synthetic procedure, structure design, composition flexibility, and customizable catalytic activity are definitely determined by adjusting the reaction atmospheres based on preparing approaches [12–14]. Furthermore, the related applications of Fe_3O_4 NPs include wide use in cancer therapy [15–18], immunotherapy [19–21], biosensors [22–24], catalysis [25–27], and drug delivery [28–30]. Therefore, it is essential to explore multifunctional or heterogeneous composites that are treated as metal enzyme mimics and maintain their catalytic activities completely.

In order to avoid the limitations of enzymatic activity, Fe_3O_4 NPs were utilized in constructing heterogeneous enzymatic agents toward various fields [13,21,25,31–34]. According to the function requirements, noble metal elements were always selected as combiners for making heterogeneous structures. They have illustrated their constructed combining complexes and additional physical or chemical properties, besides obtaining the original characteristics of magnetic composites. Regarding the individual noble metal, it gives excellent catalytic activity and optical properties because of its flexible electron transmission between metal atoms and outstanding stabilization [35–39]. Different metal forms have been used, and heterogeneous structures have been synthesized by combining them with Fe_3O_4 NPs. These heterogeneous enzyme mimics include $\text{Pd@Fe}_3\text{O}_4$ -MWCNT nanocomposite [31], $\text{Au@Fe}_3\text{O}_4$ MOF [32], Fe_3O_4 -Ag [33], and $\text{Pt-Fe}_3\text{O}_4$ [34]. These studies have discovered that doping noble metals into Fe_3O_4 NPs can improve or expand their enzymatic activities. The fundamental reason for this could be ascribed to both doped noble metals and Fe_3O_4 NPs, which have a synergetic catalysis effect and lead to the enhancement of catalytic performances. Fe_3O_4 -Ag fabrication was used in antibacterial works, and the enzymatic process also showed a synergetic catalysis effect which enhanced the antibacterial effect due to the materials' activity [19,33,40–43]. It required the high uniformity and adjusted size distribution of heterogeneous agents. The synthesis of the small size and uniformity of Fe_3O_4 -Ag require a relatively strict preparation process and harsh preparation conditions. Wei et al. [32] prepared $\text{Fe}_3\text{O}_4@MoS_2$ -Ag with a defect-rich rough surface by a Teflon-autoclave at 180 °C for 10 h and in-situ photo deposition of Ag NPs. It exhibited acceptable antibacterial performance and excellent peroxidase-like activity. Pan et al. [19] synthesized $\text{Ag}_x\text{Au}_y/\text{Fe}_3\text{O}_4$ composition via Teflon-lined stain steel autoclave, and sealed and maintained it at 150 °C for 20 h. The results showed that the activity of $\text{Ag}_x\text{Au}_y/\text{Fe}_3\text{O}_4$ NPs were improved along with increasing Ag content. The hydrophobic individual content (Fe_3O_4 and Ag NPs) exhibits negative influences while utilizing them in further biological applications [40,44]. It needed further modification in order to apply its original physical and chemical properties. In the modification procedures, the relevant properties of the enzyme were inevitably lost, and the preparation process was more complicated. This conveyed the main clues of synthetic approaches, which indicated that hydrophilic synthesis would be a preferred option in fabricating heterogeneous constructions. Therefore, the preparation of hydrophilic Fe_3O_4 and Ag composites as enzyme mimics by a simple chemical method is still a great challenge.

Herein, we reported one facile approach to make $\text{Fe}_3\text{O}_4@PEI@Ag$ structures as acceptable agents with enzymatic and photothermal properties. Heterogeneous $\text{Fe}_3\text{O}_4@PEI@Ag$ structures were fabricated by using hydrophilic Fe_3O_4 NPs as hard templates and were surface-modified by PEI molecules. Ag atoms gradually anchor on the Fe_3O_4 surface and the assembled $\text{Fe}_3\text{O}_4@PEI@Ag$ structure is constructed in water medium. Enzymatic performance was characterized as peroxidase-like activity, which verifies and illustrates in colorimetric reaction with TMB molecule. It also revealed that the heterogeneous $\text{Fe}_3\text{O}_4@PEI@Ag$ structure has a sensitive response to glucose colorimetric reactions, and can be applied to the detection of human diabetes. By subsequently coating them with ICG molecule, the $\text{Fe}_3\text{O}_4@PEI@Ag@ICG$ structure not only saw severely enhanced photothermal properties (at 808 nm irradiation) and fluorescence imaging applications [44],

but also the greatly improved stability of both parties, thanks to this combined structure. Furthermore, this heterogeneous structure could have multidirectional applications in different applications eventually.

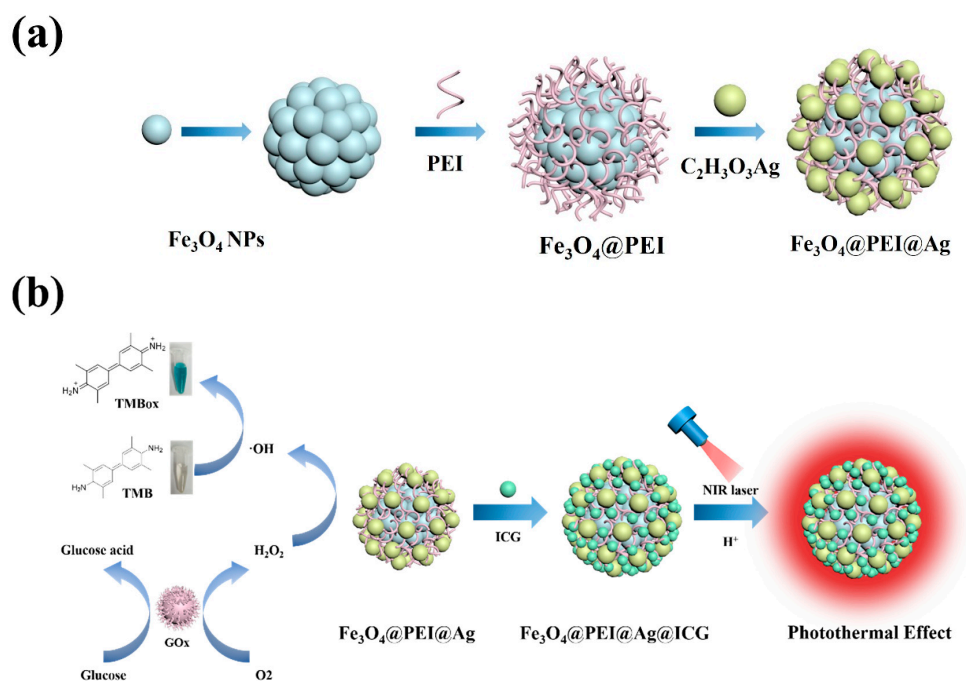
2. Results and Discussion

2.1. The Synthesis Work of $\text{Fe}_3\text{O}_4@\text{PEI@Ag}$, $\text{Fe}_3\text{O}_4@\text{PEI@Ag@ICG}$, and Relative Structural Characterizations

There are two kinds of Fe_3O_4 -based heterogeneous structures that were fabricated: $\text{Fe}_3\text{O}_4@\text{PEI@Ag}$ and $\text{Fe}_3\text{O}_4@\text{PEI@Ag@ICG}$ structures. There have unique influences on synthesis processes while using PEI and ICG molecules, respectively. In this work, the assembled structures were synthesized using a "layer-by-layer" method, as shown in Scheme 1. The characteristics of the synthesized $\text{Fe}_3\text{O}_4@\text{PEI@Ag}$ structure are depicted in Figure 1a. Firstly, the wet chemistry method was used to synthesize Fe_3O_4 and the amino-functionalized Fe_3O_4 NPs (10 nm, Figure S1a) could be obtained by using PEI for additional modifications. Further, the hydrophilic PEI with the amino group could assemble on the surface of Fe_3O_4 under mechanical stirring in order to obtain a highly dispersed $\text{Fe}_3\text{O}_4@\text{PEI}$ structure. By mediating Ag growth and anchoring it to make heterogeneous structures, PEI-mediated seed growth method was used to form $\text{Fe}_3\text{O}_4@\text{PEI@Ag}$ and $\text{Fe}_3\text{O}_4@\text{PEI@Ag@ICG}$ structures, respectively. $\text{Fe}_3\text{O}_4@\text{PEI}$ seeds were used as nucleation sites to coat the Ag by reducing silver precursors ($\text{C}_2\text{H}_3\text{O}_3\text{Ag}$). Among the deposition procedures of metal precursors, Ag seeds could immobilize on the surface of $\text{Fe}_3\text{O}_4@\text{PEI}$ through electrostatic interactions. The individual Ag seeds were approximately 10 nm (Figure S1b) and were tightly attached to the $\text{Fe}_3\text{O}_4@\text{PEI}$ surface. The main charged ability of NPs' surface can be attributed to the PEI's structural characteristics. Amino groups promoted a strong positive charge and increased the combination for assembling Fe_3O_4 and Ag completely. The diameter of the resulting $\text{Fe}_3\text{O}_4@\text{PEI@Ag}$ structure is about 150 nm and exhibited good dispersion in aqueous solution. Subsequently, the negatively charged ICG molecules were uniformly attached to the surface of $\text{Fe}_3\text{O}_4@\text{PEI@Ag}$ structure in the gap of the Ag particles. It could be thought of as one assembling procedure between two different particles (Figure 1a,b). Elemental mapping analysis was performed to confirm the elemental composition and illustrate the distribution of the $\text{Fe}_3\text{O}_4@\text{PEI@Ag}$ structure, as shown in Figure 1b–f. This proved that the assembly process can be well-realized in the form of regular aggregation.

As shown in Figure 1g, the UV-vis spectrum reflected the different optical absorbance of pure phased Fe_3O_4 , Ag, and $\text{Fe}_3\text{O}_4@\text{PEI@Ag}$ structures, respectively. Here, it is observed that this difference was obvious at the absorption spectrum, conveying that Ag showed surface plasmon resonance (SPR) at nearby 415 nm, which indicated its characteristic of a smaller diameter, less than 10 nm [43]; however, Fe_3O_4 NPs did not have a SPR effect, exhibiting a downward curve. There was an additional phenomenon in the resulting absorption of the $\text{Fe}_3\text{O}_4@\text{PEI@Ag}$ structure, which exhibited a higher SPR band at 600 nm, confirming that the Ag NPs were successfully attached to Fe_3O_4 with red-shifting phenomenon. This can be attributed to the plasmon resonance effects of the formed flower-structured Ag shell [19]. Furthermore, the SPR phenomenon appeared gradually while the $\text{Fe}_3\text{O}_4@\text{PEI@Ag}$ structure formed the accumulation of the SPR effect in a single metal and can induce new aggregation effect on structures [45]. We tried to use PVP and PEG instead of the PEI molecule in characterization, as shown in Figure S2. When PVP was used, it could link Ag and Fe_3O_4 together, but the UV characteristic peak at 415 nm disappeared after being left for some time, which proved that using PVP as the linker was not stable. When PEG was used, there was no characteristic also in optical measurements, which might prove that PEG was not suitable as a linker for Fe_3O_4 and Ag additionally. XRD characterization was applied to analyze the crystalline structure of Fe_3O_4 and $\text{Fe}_3\text{O}_4@\text{PEI@Ag}$ NPs, as shown in Figure 1h. The XRD pattern of the Fe_3O_4 NPs showed six characteristic diffraction peaks at 30.1° , 35.5° , 43.3° , 53.7° , 57.2° , and 62.8° corresponding to the (220), (311), (400), (422), (511), and (440) crystal planes of pure magnetite (Fe_3O_4) with a cubic

spinel structure (JCPDS card. No. 03-065-3107). The high crystallinity of the Fe_3O_4 was evident from the sharp diffraction pattern peaks. On the other hand, the XRD pattern of $\text{Fe}_3\text{O}_4@PEI@Ag$ was similar to that of Fe_3O_4 particle, and the pattern of the $\text{Fe}_3\text{O}_4@PEI@Ag$ shows additional peaks at 2θ values of 38.1° , 44.3° , 64.5° , 77.4° , corresponding to the reflections of the (111), (200), (220), (311) crystalline planes, respectively, of the face-central cubic crystal structure of Ag. The above result was consistent with ASTM standard (JCPDS Card No. 04-0783) and further confirmed that the Ag on the surface of the composite structure exists in the zero-valent state. FT-IR is an appropriate technique to study chemical adsorption or chemical interaction [44]. As shown in Figure 1i, FT-IR spectrum conveyed the pure Fe_3O_4 , $\text{Fe}_3\text{O}_4@PEI$, and $\text{Fe}_3\text{O}_4@PEI@Ag$ structure, respectively. According to Fe_3O_4 particles, the peak around 577 cm^{-1} belonged to Fe-O vibration [45]. The peak absorption bands at 3405 cm^{-1} and 1627 cm^{-1} correspond to the O-H stretching vibration and bending vibration, respectively [46–48]. After PEI is coated on the surface of Fe_3O_4 , the peak at 1546 cm^{-1} in the $\text{Fe}_3\text{O}_4@PEI$ curve represents the N-H asymmetric bending vibration peak, and the Fe-O stretch at 577 cm^{-1} was obviously weakened. The appearance and vibrations of the functional groups indicated that the Fe_3O_4 NPs were modified by PEI through a covalent bond [49]. Meanwhile, the incorporation of Ag did not change the structures of the composites. All of the above implied the linkage between particles and molecules were exactly impressed.



Scheme 1. (a) The schematic diagram of the synthesis of the $\text{Fe}_3\text{O}_4@PEI@Ag$ structure; (b) the detailed procedures and processes of new insights into the assembled $\text{Fe}_3\text{O}_4@PEI@Ag$ structure as an acceptable agent with enzymatic and photothermal properties.

We aimed toward a $\text{Fe}_3\text{O}_4@PEI@Ag$ structure, which could be considered as a magnetic carrier. Conventionally, a magnetic carrier is useful for directing the spatial distribution of drugs via noninvasive magnetic guiding. To investigate the magnetic response of the Fe_3O_4 and $\text{Fe}_3\text{O}_4@PEI@Ag$ structure, the magnetic properties of different samples were investigated at 300 K and the superparamagnetism of $\text{Fe}_3\text{O}_4@PEI@Ag$ had a lower saturation magnetization of $8.50\text{ emu}\cdot\text{g}^{-1}$ compared to the pure Fe_3O_4 ($57.04\text{ emu}\cdot\text{g}^{-1}$). The reduced magnetism of $\text{Fe}_3\text{O}_4@PEI@Ag$ structure was due to the compact shielding of nonmagnetic PEI and Ag on the Fe_3O_4 surface, which could be explained by the lower mass ratio of Fe_3O_4 in-unit composites [50]. Additionally, we used a magnet placed next to the sidewall of a cuvette containing an aqueous dispersion ($10\text{ mg}\cdot\text{mL}^{-1}$) of $\text{Fe}_3\text{O}_4@PEI@Ag$. It can rapidly migrate toward the magnet and is accumulated against the inner wall within

1 min (the Fe_3O_4 NPs just needed 30 s) as illustrated in Videos S1 and S2, and they could be dispersed again homogeneously if the magnet was removed (Figure 2a). Figure 2b showed the changes in the ζ -potential measurement of each component while mediating with Fe_3O_4 , which can monitor the modification in fabricating assembled $\text{Fe}_3\text{O}_4@PEI@Ag$ structures. In detail, the changes in surface potential from negative to positive after PEI coated, which demonstrated the successful assembly of cationic PEI on Fe_3O_4 NPs by electrostatic interaction. At same time, the zeta potential value changed from -17.99 mV to $+20.70$ mV. Once Ag was adhered to formation, it could increase to $+25.11$ mV, which proved the dispersion ($\text{Fe}_3\text{O}_4@PEI@Ag$ structure) was improved compared to $\text{Fe}_3\text{O}_4@PEI$ completely. Similarly, the zeta potential turned negative again ($+25.11$ mV to -14.95 mV) due to the successful conjugation of negatively charged ICG molecules on the surface of the $\text{Fe}_3\text{O}_4@PEI@Ag$ structure. In the PBS environment, it can improve the dispersion of the $\text{Fe}_3\text{O}_4@PEI@Ag@ICG$ structure (-14.95 mV to -22.21 mV). Before and after being modified by the ICG molecule, the stability of the $\text{Fe}_3\text{O}_4@PEI@Ag$ structure was also tested as shown in Figure S3; it maintained good dispersion in solvent even after 48 h of culturing.

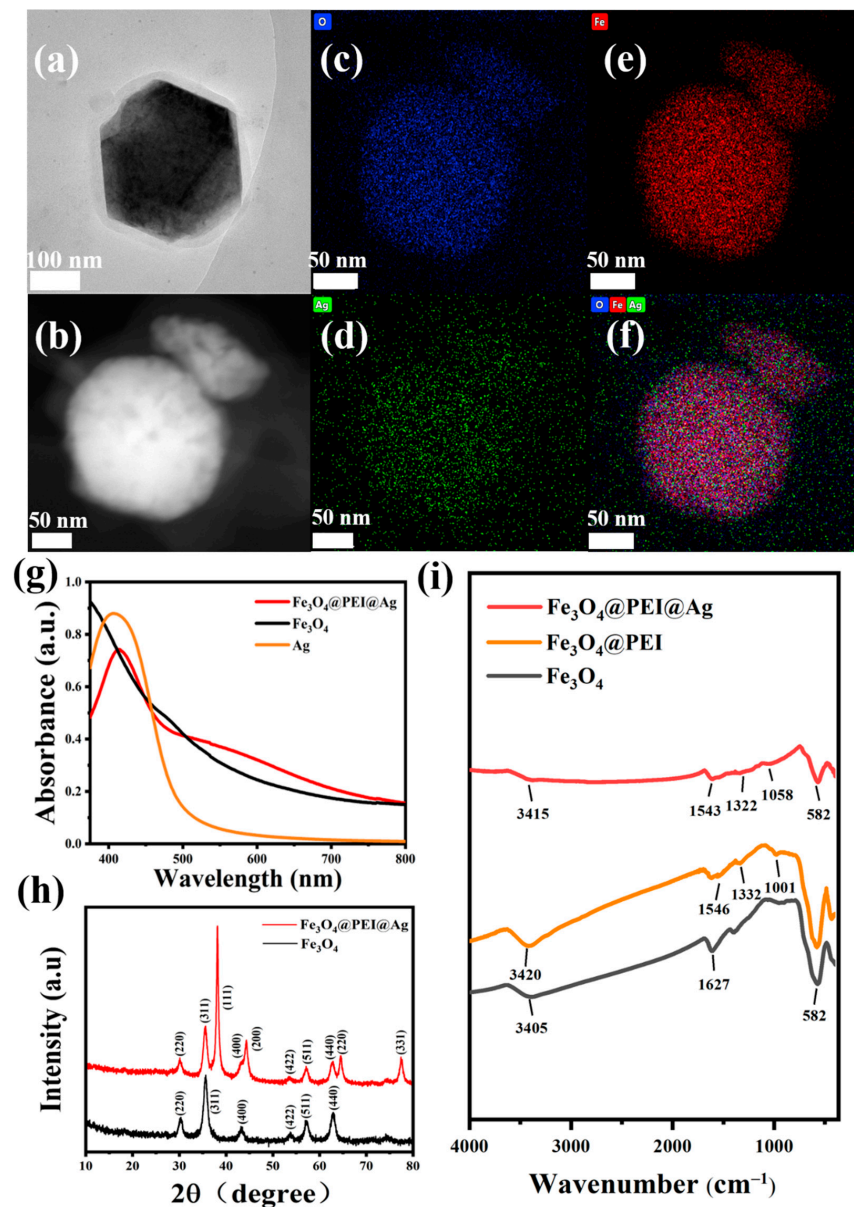


Figure 1. The characterization of the synthesized $\text{Fe}_3\text{O}_4@PEI@Ag$ structure: (a) the TEM images of $\text{Fe}_3\text{O}_4@PEI@Ag$ structure; (b) the dark field TEM image and (c–f) the elemental mapping images

of Fe, O, Ag composition, respectively; (g) UV-vis absorbance spectra of each Fe_3O_4 , Ag, and $\text{Fe}_3\text{O}_4@PEI@Ag$ structure, in DI water medium; (h) powder XRD patterns of Fe_3O_4 and $\text{Fe}_3\text{O}_4@PEI@Ag$; (i) FT-IR spectra of Fe_3O_4 , $\text{Fe}_3\text{O}_4@PEI$, and $\text{Fe}_3\text{O}_4@PEI@Ag$ structure.

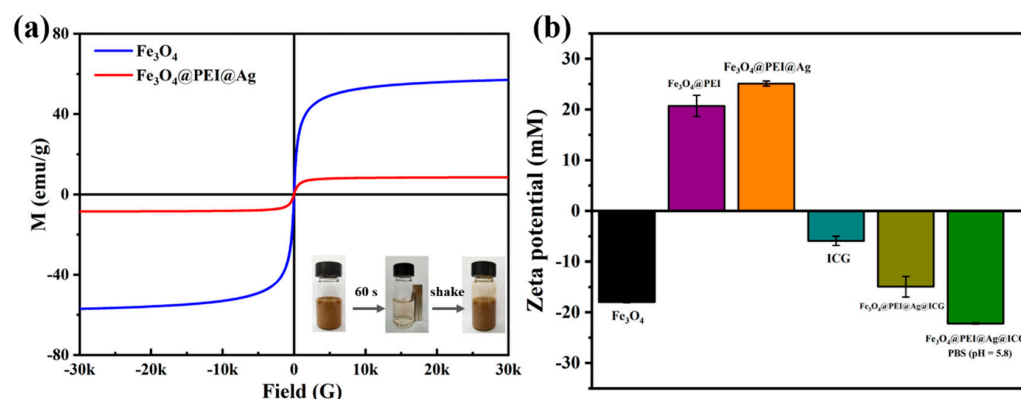


Figure 2. (a) Magnetic properties of Fe_3O_4 and $\text{Fe}_3\text{O}_4@PEI@Ag$ structure (300 K), and the inset image is the checking in outer magnetism functions. (b) Zeta potentials of the intermediate and final product.

2.2. Peroxidase-like Activity of Assembled $\text{Fe}_3\text{O}_4@PEI@Ag$ Structure

Originally, Fe_3O_4 NPs possess intrinsic peroxidase-like activities under acidic conditions in previous studies [7]. The typical reaction of TMB and H_2O_2 were used to investigate the peroxidase-like activity of $\text{Fe}_3\text{O}_4@PEI@Ag$ structure. As shown in Figure 3a, pure phased Fe_3O_4 ($100 \mu\text{L}$, $100 \mu\text{g}\cdot\text{mL}^{-1}$), Ag ($100 \mu\text{L}$, $100 \mu\text{g}\cdot\text{mL}^{-1}$), and $\text{Fe}_3\text{O}_4@PEI@Ag$ structure ($100 \mu\text{L}$, $100 \mu\text{g}\cdot\text{mL}^{-1}$) were measured to check their characteristics after reaction with H_2O_2 ($100 \mu\text{L}$, 1 mM) and TMB ($100 \mu\text{L}$, 1 mM) within 10 min (UV-vis spectra). The inset images showed typical digital images of each colloidal solution. The peaks matched, being nearly about 652 nm , which implied the intrinsic peroxidase-mimicking activity of each colloidal solution [51,52]. It implied that the catalytic reaction to oxidize TMB corresponded to TMB_{ox} by H_2O_2 . Comprehensively, the typical absorbance at 652 nm was observed with 5 min incubations, which is completely different from control works. In these, the target TMB could not show any changes in colors. It is worth noting that the $\text{Fe}_3\text{O}_4@PEI@Ag$ structure enhanced peroxidase-like activity, even as each (Fe_3O_4 and Ag) exhibited relative catalytic properties. Here, the higher catalytic performance could be ascribed to synergistic effects from the assembling process of Fe_3O_4 and Ag NPs. This enzymatic property was investigated under different pH conditions. As shown in Figure S4a, pure Fe_3O_4 NPs were firstly studied in the catalytic reaction of the TMB vs. pH value, and they exhibited catalytic activity only at $\text{pH} = 5.8$. Likewise, the $\text{Fe}_3\text{O}_4@PEI@Ag$ structure exhibited the highest catalytic performance at $\text{pH} = 5.8$ as shown in Figure 3b. With the increasing pH or the decreasing pH, the relative activity of the $\text{Fe}_3\text{O}_4@PEI@Ag$ structure decreased even without enzyme activity. The peroxidase-like activities of $\text{Fe}_3\text{O}_4@PEI@Ag$ structure could gradually be enhanced by increasing the amount of the catalyst, as shown in Figure 3c. We found that the reaction rate of TMB oxidation was highly dependent on the amount of $\text{Fe}_3\text{O}_4@PEI@Ag$ structure. In Figure 3d, the strong absorbance at 652 nm could well prove the advanced catalytic reaction within 30 min at RT, and it exhibited the catalytic performance of the assembled $\text{Fe}_3\text{O}_4@PEI@Ag$ structure. The intensity of this was recorded and is shown in Figure S4b. As the reaction time increased, the oxidation products in the products could gradually accumulate together more than before.

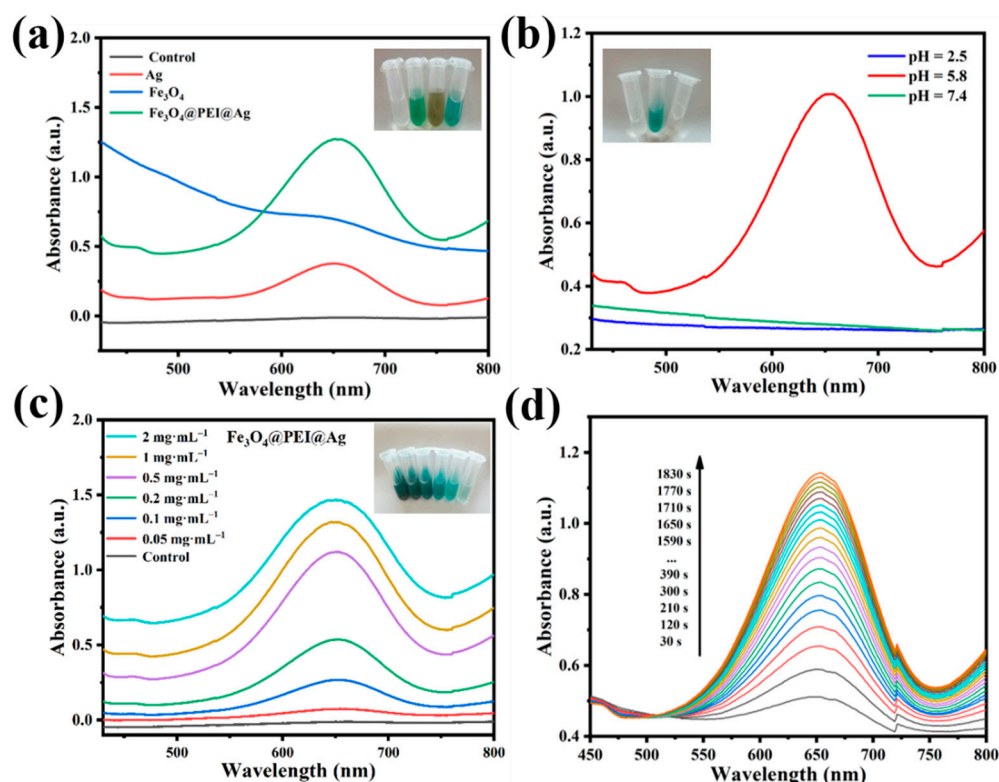


Figure 3. (a) UV-vis spectra and digital images (inset) of TMB catalyzed by the Fe_3O_4 , Ag, and $\text{Fe}_3\text{O}_4@PEI@Ag$ structure in the presence of H_2O_2 . (b) Effect of pH on the peroxidase-like activity of $\text{Fe}_3\text{O}_4@PEI@Ag$ structure. (c) The peroxidase-like activity of $\text{Fe}_3\text{O}_4@PEI@Ag$ structure at different concentrations: 0.05, 0.1, 0.2, 0.5, 1 and $2 \text{ mg}\cdot\text{mL}^{-1}$, respectively. (d) The catalytic performance was achieved during in 30 min.

2.3. Steady-State Kinetic Assay of $\text{Fe}_3\text{O}_4@PEI@Ag$ Structure

The Michaelis–Menten equation was used to investigate the kinetics of the catalytic process due to the excessive H_2O_2 that can inhibit the reaction progress. The concentration was restricted to a certain range of Michaelis–Menten curves of two catalysts (Figure 4). It estimated the peroxidase-like activities while keeping H_2O_2 or TMB as the unique variable in reactions. It showed that the catalytic activity gradually increased along with the concentration of H_2O_2 or TMB, as shown in Figure 4a,b. When the substrate concentration was low, the reaction products showed a rapid growth stage along with the increase in substrate concentration. With the increase in substrate concentration, the change in the absorption peak gradually became slow. In Figure 4c,d, an increase tendency in catalytic property once the concentration of H_2O_2 and TMB reached 20 mM and 6 mM, respectively, can be observed. This illustrated the higher quantities of H_2O_2 (>20 mM) and resulted in a reaction limit. Due to the no longer increased catalytic activities, in which the competed procedure could be induced while a single catalytic site met the higher concentration of TMB and H_2O_2 [50]. Similarly, relative activity rose steadily as TMB concentration rose, eventually reaching a plateau at greater TMB concentrations. In order to investigate the kinetic study of the catalytic process in our work, it was analyzed according to the Michaelis–Menten equation. The apparent steady-state kinetic parameters K_m (Michaelis–Menten constant), K_{cat} (turnover number) and V_{max} (the maximal reaction velocity) were set up in further estimation. The lower K_m , which is equivalent to the substrate concentration in which the rate of conversion is half of V_{max} , represents the higher affinity between the catalyst and the substrate. The higher K_{cat} , which is obtained by dividing V_{max} by the catalyst concentration, refers the higher rate of enzyme catalysis under the best conditions [53,54]. A series of initial rates (V_0) of TMB oxidation were

calculated from the time-dependent absorption values at 652 nm. The absorption value of the oxidized TMB product was converted to concentration by Equation (1) [39]:

$$[\text{TMB}_{\text{ox}}] = \frac{A}{\sum_{[\text{TMB}_{\text{ox}}]} \times L} \quad (1)$$

where $[\text{TMB}_{\text{ox}}]$ denotes the TMB_{ox} concentration, A is the UV-absorbance, L is the solution thickness (1 cm), and $\sum_{[\text{TMB}_{\text{ox}}]}$ shows the molar absorption coefficient, having the value of $39,000 \text{ M}^{-1} \cdot \text{cm}^{-1}$ for the TMB_{ox} product at 652 nm. By using the above equation we can obtain the value of TMB_{ox}.

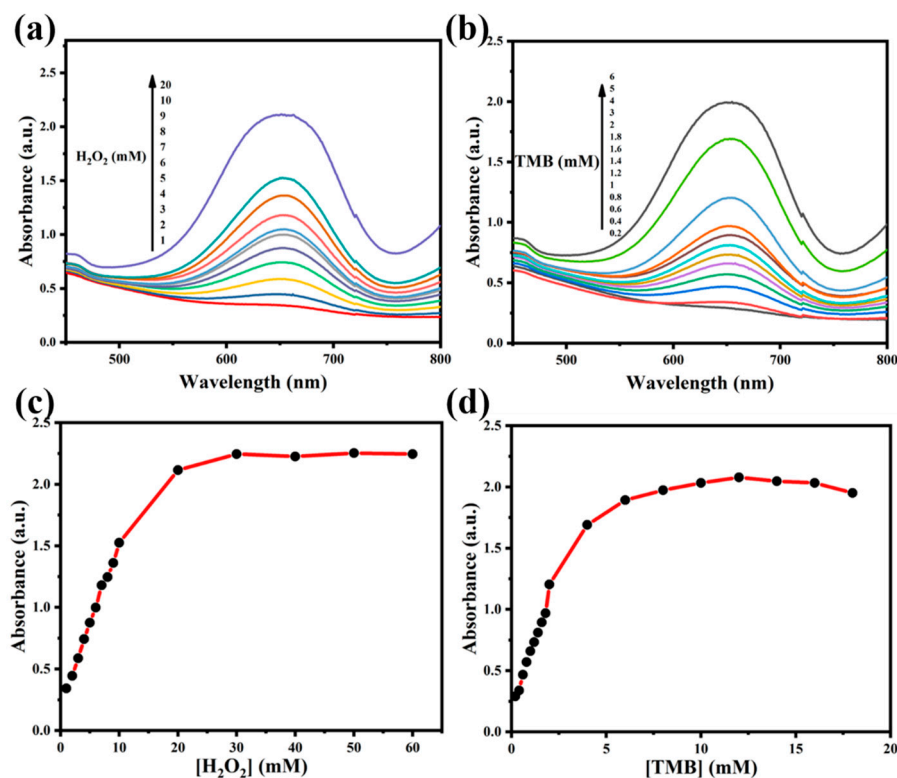


Figure 4. (a,b) UV-vis absorption spectra and (c,d) absorbance of assembled $\text{Fe}_3\text{O}_4@PEI@Ag$ structure ($200 \mu\text{g} \cdot \text{mL}^{-1}$) incubated at different concentrations of (a,c) H_2O_2 and (b,d) TMB for 10 min.

The plotting of the beginning rates against TMB or H_2O_2 concentrations yielded the classic Michaelis–Menten curves. The data were analyzed by the Lineweaver–Burk or double reciprocal plot ($\frac{1}{V_0}$ vs $\frac{1}{[S]}$) using Equation (2) [53]. The slope and intercepts of the relevant linear graphs were used to compute the Michaelis–Menten parameters (K_m) and the maximal reaction velocity (V_{max}) values. Further, K_m and V_{max} for H_2O_2 and TMB were obtained from the reciprocal negative x-intercept and reciprocal y-intercept, respectively. The turnover number (K_{cat}) for H_2O_2 and TMB were obtained from Equation (3) (Table 1).

$$\frac{1}{V_0} = \frac{K_m}{V_{\text{max}}[S]} + \frac{1}{V_{\text{max}}} \quad (2)$$

$$K_{\text{cat}} = V_{\text{max}}/[S] \quad (3)$$

where V_0 represents the initial velocity, $[S]$ refers to the concentration of substrate.

Figure 5a,b showed that the peroxidase-like activity of $\text{Fe}_3\text{O}_4@PEI@Ag$ follows a classic Michaelis–Menten enzyme behavior. The double reciprocal of the initial rate (V_0)

versus the substrate concentrations in Figure 5c,d gave an excellent linear relationship. Equations (4) and (5) are the linear regression equations.

$$\frac{1}{V_0} = 0.918 \times 10^8 \frac{1}{[\text{H}_2\text{O}_2]} + 0.077 \times 10^8, R^2 = 0.993 \quad (4)$$

$$\frac{1}{V_0} = 0.260 \times 10^8 \frac{1}{[\text{TMB}]} + 0.086 \times 10^8, R^2 = 0.988 \quad (5)$$

Table 1. Kinetic parameters of the Fe₃O₄@PEI@Ag structure.

[S] (mg·mL ⁻¹)		K _m (mM)		K _{cat} (×10 ⁻¹⁰ mol·s ⁻¹ ·mg ⁻¹)		V _{max} (×10 ⁻⁷ M·s ⁻¹)	
Fe ₃ O ₄ @PEI@Ag	0.2	H ₂ O ₂	TMB	H ₂ O ₂	TMB	H ₂ O ₂	TMB
		1.192	0.302	6.495	5.815	1.299	1.163

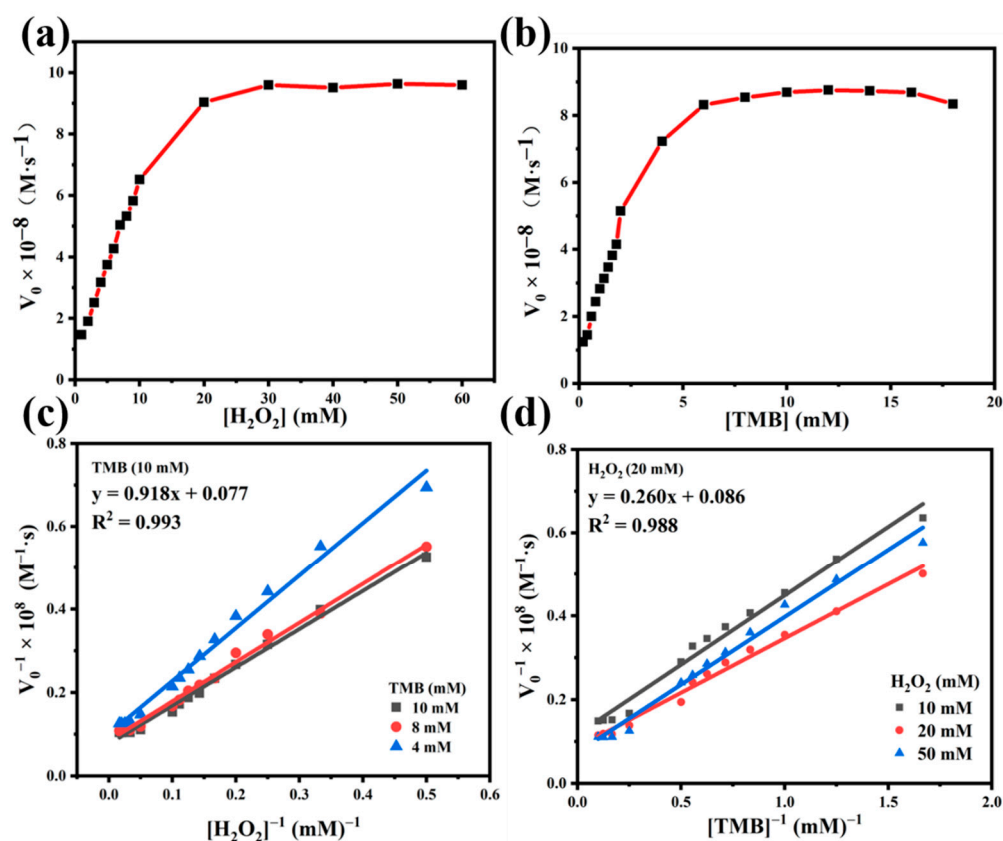


Figure 5. Steady-state kinetic assay and catalytic ability of Fe₃O₄@PEI@Ag structure: (a,c) toward [H₂O₂], (b,d) toward [TMB].

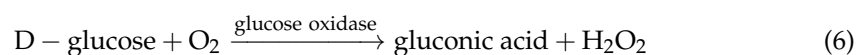
For overall consideration, the comparisons with others enzymatic and HRP catalytic performance as shown in Table S1 [55–60]. This assembled Fe₃O₄@PEI@Ag structure has high affinity for both target agents due to their huge surface area and multiple active catalytic sites. In Figure 5c,d, the K_m values of 1.192 mM and 0.302 mM were obtained for H₂O₂ and TMB, respectively. The apparent K_m of the Fe₃O₄@PEI@Ag structure with H₂O₂ as the substrate was about three times lower than HRP, suggesting that the Fe₃O₄@PEI@Ag structure have a higher affinity for H₂O₂ than HRP. The K_m value of Fe₃O₄@PEI@Ag structure for TMB was also lower than HRP. This suggested a high affinity and prominent catalytic activity. The advantages of Fe₃O₄@PEI@Ag structure in catalytic efficiency were also identified since their K_{cat} values for H₂O₂ and TMB were 6.495 × 10⁻¹⁰ mol·s⁻¹·mg⁻¹ and 5.815 × 10⁻¹⁰ mol·s⁻¹·mg⁻¹. The V_{max} of Fe₃O₄@PEI@Ag structure with H₂O₂ as

substrate ($1.299 \times 10^{-7} \text{ M}\cdot\text{s}^{-1}$) and TMB as the substrate ($1.163 \times 10^{-7} \text{ M}\cdot\text{s}^{-1}$) were higher than HRP ($0.87 \times 10^{-7} \text{ M}\cdot\text{s}^{-1}$ and $1 \times 10^{-7} \text{ M}\cdot\text{s}^{-1}$) [61]. By comparing with previous FePt-Au, CuO-Au, GBR, and ZnFe₂O₄ [62–64] structures, the Fe₃O₄@PEI@Ag structure exhibits better enzymatic affinity and peroxidase-like catalytic performance than previously reported metal or metal-based enzyme mimics. The kinetic studies showed that the peroxidase-like activity of the Fe₃O₄@PEI@Ag structure is advantageous compared to that of HRP and other previously reported enzyme mimics.

The slope and intercepts of the relevant liner graphs were used to compute the K_m and V_{max} values. For overall consideration, the comparisons with other enzymatic and HRP catalytic performances are shown in Table S1. This assembled Fe₃O₄@PEI@Ag structure has high affinity for both target agents due to their huge surface area and multiple active catalytic sites. In Figure 5c,d, it could be seen from Equation (2) that the K_m values of 1.192 mM and 0.302 mM were obtained for H₂O₂ and TMB, respectively. The K_m values were lower for HRP than for the Fe₃O₄@PEI@Ag structure treated with H₂O₂ and TMB, which suggests its high affinity and prominent catalytic activity. The V_{max} of Fe₃O₄@PEI@Ag structure with H₂O₂ as substrate ($1.299 \times 10^{-7} \text{ M}\cdot\text{s}^{-1}$) and TMB as the substrate ($1.163 \times 10^{-7} \text{ M}\cdot\text{s}^{-1}$) were higher than HRP ($0.87 \times 10^{-7} \text{ M}\cdot\text{s}^{-1}$ and $1 \times 10^{-7} \text{ M}\cdot\text{s}^{-1}$) [61]. The specific values could be exactly achieved. By comparing them with the previous FePt-Au, CuO-Au, GBR, and ZnFe₂O₄ [62–64], the Fe₃O₄@PEI@Ag structure exhibit better enzymatic affinity and peroxidase-like catalytic performance than previously reported metal or metal-based enzyme mimics. The kinetic studies showed that the peroxidase-like activity of Fe₃O₄@PEI@Ag structure is superior to that of HRP and other previously reported enzyme mimics.

2.4. Colorimetric Detection of Glucose and Cytotoxicity Measurement of Fe₃O₄@PEI@Ag and Fe₃O₄@PEI@Ag@ICG

In clinical diagnosis, the glucose content of urine or blood samples is important in the evaluation of the health or physical condition of a patient. As H₂O₂ is the intermediate of the glucose oxidation reaction that is catalyzed by GOx, H₂O₂ sensing can provide great assistance to the colorimetric detection of glucose [55]. The mechanism for the detection is as follows:



The detection of glucose was realized based on the peroxidase-like activity. Fe₃O₄@PEI@Ag was evaluated for their potential application as mimics of HRP in glucose detection. Firstly, 100 μL glucose solution was used, with different concentrations ranging from 1 μM to 500 μM in buffer (300 μL , PH 7.4), and these were incubated with glucose oxidase (100 μL , 10 $\text{mg}\cdot\text{mL}^{-1}$) at 37 °C for 30 min. Next, the required amount of Fe₃O₄@PEI@Ag (100 μL , 1 $\text{mg}\cdot\text{mL}^{-1}$) and TMB (100 μL , 10 mM) were added in the buffer solutions (300 μL , PH 5.8). A corresponding absorbance (652 nm) would be recorded, and the diagram of colorimetric difference exhibited the detection of glucose, eventually (the inset image in Figure 6a). Furthermore, the data was used to draw a linear calibration plot ($y = 1.876x + 0.008$, $R^2 = 0.997$) (Figure S5). Compared to previous references, Fe₃O₄@PEI@Ag has a better linear range and low detection limit [65–68]. Lactose, sucrose, fructose, and maltose were used to investigate the selectivity of this biosensing system, as control samples. Observed from Figure 6b, the glucose (0.5 mM) generated stronger response than the controlled samples (5 mM), reaching a 5-fold higher value.

For verification, cytotoxicity measurement was preliminarily monitored, as shown in Figure 6c,d. The vitality of cells was measured in relation to agent concentration for evaluating cytotoxicity. The effect of Fe₃O₄@PEI@Ag and Fe₃O₄@PEI@Ag@ICG on Hacat cells was evaluated by MTT assay with different colloidal solutions. There was no reduction of cell viability observed for Hacat cells that were treated with various concentrations (5–200 $\mu\text{g}\cdot\text{mL}^{-1}$) and that underwent incubation for 24 h. Cell viability above 80%

means placement in the category of biocompatible materials [69]. Thus, the synthesized $\text{Fe}_3\text{O}_4@PEI@Ag$ structure can be considered as a nontoxic and biocompatible agent.

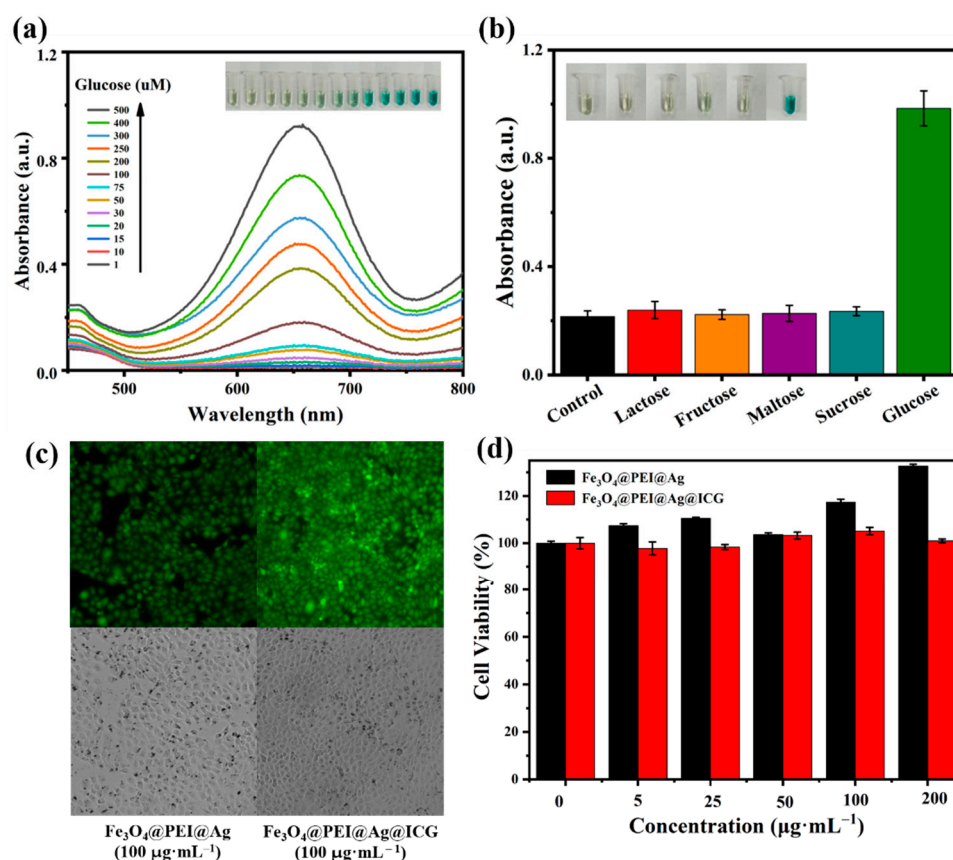


Figure 6. (a) UV-*vis* absorption spectra of the sensing system toward glucose with various concentrations. The inset image showed the corresponding color changes. (b) The selectivity of glucose determination with 5 mM other carbohydrates and 0.5 mM glucose. Insert image shows the color change of different solutions. (c) The images of representative fluorescence and optical microscopy with colloidal solution ($100 \mu\text{g}\cdot\text{mL}^{-1}$). (d) The Hacat cell viability of each sample with different colloidal concentrations ($5\text{--}200 \mu\text{g}\cdot\text{mL}^{-1}$) after 24 h.

2.5. Photothermal Property of $\text{Fe}_3\text{O}_4@PEI@Ag@ICG$ Structure

The Vis-NIR spectra showed strong and broad absorbance of $\text{Fe}_3\text{O}_4@PEI@Ag$ structure at 700–900 nm (Figure 7a), suggesting its remarkable potential as a photothermal agent. By being coated with photosensitizer, the enhancement of the corresponding photothermal property might be induced. ICG could enhance the original property of assembled structures; the typical absorbance peak of $\text{Fe}_3\text{O}_4@PEI@Ag@ICG$ was at 870 nm (NIR-I, 700–1000 nm). This implied a gradual red-shift by comparing it with pure ICG (780 nm), a change that can be ascribed to the formation of ICG dimers or oligomers, also known as J-aggregates [70]. The intensity was positively correlated with the concentration of $\text{Fe}_3\text{O}_4@PEI@Ag@ICG$, indicating their mono-dispersion in aqueous conditions (Figure 7b). At the same time, we also explored the near-infrared absorption values of Fe_3O_4 NPs and $\text{Fe}_3\text{O}_4@PEI@Ag$ with different concentrations (Figure S6a,b). Their absorption values increased along with concentration increasing, which showed the same phenomenon as before.

An NIR laser of 808 nm ($1 \text{ W}\cdot\text{cm}^{-2}$) was used to activate the photothermal properties. The $\text{Fe}_3\text{O}_4@PEI@Ag@ICG$ dispersion ($200 \mu\text{L}$, $200 \mu\text{g}\cdot\text{mL}^{-1}$) was subject to laser irradiation for 5 min, and the temperature variation was recorded every 20 s in order to evaluate the photothermal phenomenon (Figure 7c). The temperature of the DI water, Fe_3O_4 NPs,

$\text{Fe}_3\text{O}_4@PEI@Ag$ structure, and Free ICG were increased by 1.6, 4.3, 7.7, and 13.3 °C, respectively, which implied an insignificant photothermal effect. In contrast, a remarkable temperature elevation was observed in $\text{Fe}_3\text{O}_4@PEI@Ag@ICG$ with increments of 21.6 °C under same treatment. This can be attributed to the remarkable photothermal response of the conjugated ICG molecules. Additionally, the temperature elevation of the $\text{Fe}_3\text{O}_4@PEI@Ag$ structure and the $\text{Fe}_3\text{O}_4@PEI@Ag@ICG$ dispersion was concentration-dependent, as shown in Figures 7d and S6c. The temperature increased over time in $\text{Fe}_3\text{O}_4@PEI@Ag@ICG$ suspensions, which also exhibited laser output power density-dependent profiles (Figure S6d).

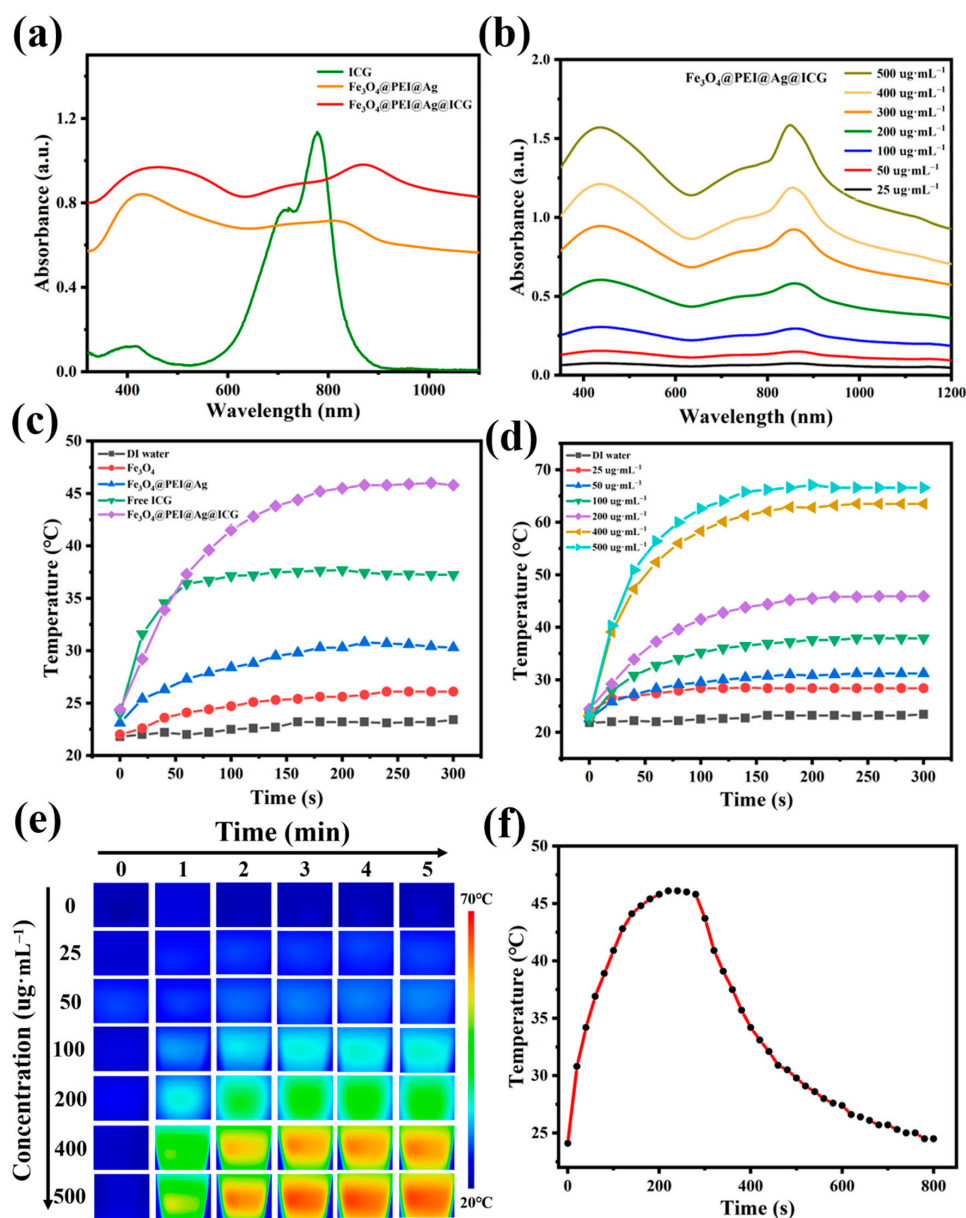


Figure 7. (a) Vis-NIR absorbance spectral of $\text{Fe}_3\text{O}_4@PEI@Ag$ structure, ICG, and $\text{Fe}_3\text{O}_4@PEI@Ag@ICG$ while dispersed in aqueous solution. (b) The Vis-NIR spectrum of $\text{Fe}_3\text{O}_4@PEI@Ag@ICG$ dispersion with different concentrations. (c) Temperature change in various solutions (200 $\mu\text{g}\cdot\text{mL}^{-1}$) over 5 min of NIR laser irradiation recorded by a digital thermometer. (d) Temperature response of $\text{Fe}_3\text{O}_4@PEI@Ag@ICG$ dispersion with gradient concentrations under NIR laser irradiation. (e) The Infrared thermal images of cuvettes containing the $\text{Fe}_3\text{O}_4@PEI@Ag@ICG$ dispersion to show the temperature change over time under different concentrations corresponding to (d) (laser wavelength: 808 nm; laser power: 1 $\text{W}\cdot\text{cm}^{-2}$). (f) Temperature changes of $\text{Fe}_3\text{O}_4@PEI@Ag@ICG$ (200 $\mu\text{g}\cdot\text{mL}^{-1}$) underwent one consecutive heating-cooling cycle 15 min under NIR laser irradiation.

The temperature of the $\text{Fe}_3\text{O}_4@\text{PEI}@\text{Ag}@\text{ICG}$ dispersion during laser irradiation was also monitored in real time by infrared imaging (Figure 7e). Such a notable photothermal effect of the $\text{Fe}_3\text{O}_4@\text{PEI}@\text{Ag}@\text{ICG}$ structure may facilitate thermographic imaging in vivo during photothermal therapy (PTT). The stability was evaluated by applying repetitive laser irradiation and cooling (15 min for one cycle) (Figure 7f). Significantly, the $\text{Fe}_3\text{O}_4@\text{PEI}@\text{Ag}@\text{ICG}$ has a faster photothermal response, which can rise to the temperature limit in 3.5 min, and can quickly decrease to RT after removing the Laser. This is more sensitive than that of the widely used PTT agents, such as gold nano shells (5 min and 11 min) [43], copper sulfide (10 min and 10 min) [71], and polydopamine nanoparticles (10 min and 20 min) [72].

3. Materials and Methods

3.1. Materials

Iron (II) chloride tetrahydrate ($\text{FeCl}_2 \cdot 4\text{H}_2\text{O}$, 98%) and Silver acetate ($\text{C}_2\text{H}_3\text{O}_3\text{Ag}$, 99.5%) were purchased from Sigma-Aldrich Co., Ltd. (St. Louis, MI, USA). Iron chloride hexahydrate ($\text{FeCl}_3 \cdot 6\text{H}_2\text{O}$, 99%), Sodium citrate tribasic dihydrate ($\text{C}_6\text{H}_5\text{Na}_3\text{O}_7 \cdot 2\text{H}_2\text{O}$, $\geq 99\%$), Polyethyleneimine ethylenediamine branched (PEI, average weight 800), PEG-400 ($\text{HO}(\text{CH}_2\text{CH}_2\text{O})_n\text{H}$), average weight 400(MW)), Polyvinylpyrrolidone (PVP, average weight 360,000), Ammonium hydroxide solution ($\text{NH}_3 \cdot \text{H}_2\text{O}$), 3,3',5,5'-Tetramethylbenzidine (TMB, 240.35(MW)), Sucrose ($\text{C}_{12}\text{H}_{22}\text{O}_{11}$, 342.30(MW)), D-(+)-Maltose monohydrate ($\text{C}_{12}\text{H}_{22}\text{O}_{11} \cdot \text{H}_2\text{O}$, 360.31(MW)), D-Fructose ($\text{C}_6\text{H}_{12}\text{O}_6$, 180.16(MW)), Glucose Oxidase from *Aspergillus niger* (GOx, 100 U/mg), Dimethyl sulfoxide (DMSO, 78.13(MW)), Phosphate buffer (pH 5.8), phosphate-buffered saline (PBS, pH 7.4), and Indocyanine green (ICG) were supplied by Aladdin Reagent Co., Ltd. (Shanghai, China), D-Glucose ($\text{C}_6\text{H}_{12}\text{O}_6 \cdot \text{H}_2\text{O}$, 198.17) were provided by KESHI (Chengdu, China), α -Lactose ($\text{C}_{12}\text{H}_{22}\text{O}_{11} \cdot \text{H}_2\text{O}$, 360.31(MW)) were obtained from Kermel (Tianjin, China). Ultrapure water utilized throughout the study was produced using a Milli-Q water purification system.

3.2. Preparation of Fe_3O_4 NPs

Firstly, Fe_3O_4 NPs were prepared via a chemical co-precipitation method [42], with slight changes. Briefly, $\text{FeCl}_2 \cdot 4\text{H}_2\text{O}$ (0.19881 g) and $\text{FeCl}_3 \cdot 6\text{H}_2\text{O}$ (0.5406 g) were solved in 100 mL of deionized water with a molar ratio of 1:2 in a triple-neck round-bottom flask. then sonicated for 20 min. The mixture was then heated in a water bath and stirred magnetically. The reaction temperature was then raised to 80 °C, and the solution was allowed to react for 30 min under continuous stirring. In the meantime, when water was heated to 30 °C, Ammonium hydroxide solution ($\text{NH}_3 \cdot \text{H}_2\text{O}$) (8 mL) was added. When the temperature reached 40 °C, Sodium citrate tribasic dihydrate ($\text{C}_6\text{H}_5\text{Na}_3\text{O}_7 \cdot 2\text{H}_2\text{O}$, 2.94 g) was added. The resulting black precipitate, obtained by cooling the reaction mixture to room temperature, was thoroughly rinsed with copious amounts of water several times. The precipitate was separated from the supernatant after each rinsing step using a permanent magnet. Finally, the black-colored precipitate was dried in a vacuum oven at 60 °C overnight.

3.3. Preparation of $\text{Fe}_3\text{O}_4@\text{PEI}@\text{Ag}$ and $\text{Fe}_3\text{O}_4@\text{PEI}@\text{Ag}@\text{ICG}$ Structures

A one-step method was used to prepare the $\text{Fe}_3\text{O}_4@\text{PEI}@\text{Ag}$ structure, which comprised the formation of silver seeds on the surface of $\text{Fe}_3\text{O}_4@\text{PEI}$ NPs and the formation of silver nanoparticles reduced by glucose. Firstly, Fe_3O_4 (0.0578 g) and glucose (2.25 g) were dissolved in 40 mL deionized water in a triple-neck round-bottom flask, then sonicated for 20 min. The mixture was heated and stirred in a water bath, and the reaction temperature was then raised to 100 °C. After that, 10 mL PEI aqueous solution ($0.1 \text{ g} \cdot \text{mL}^{-1}$) was added to the mixture. We also tried to use PVP (10 mL, $0.06 \text{ g} \cdot \text{mL}^{-1}$) and PEG (10 mL, $0.2 \text{ g} \cdot \text{mL}^{-1}$) as substitutes for PEI. After 30 min, 10 mL of silver acetate was added to the mixture. The reaction temperature was maintained at 100 °C for 2 h with slow magnetic stirring. Afterwards, heating was stopped and stirring continued until the mixture cooled to room temperature. The products were collected with a magnet and washed with Milli-Q water

several times. Finally, the black-colored precipitate was dried in a vacuum oven at 37 °C overnight for further use.

A total of 5 mL dispersion of Fe₃O₄@PEI@Ag (20 mg·mL⁻¹) was mixed with 20 mL of ICG aqueous solution (100 µg·mL⁻¹) and stirred at room temperature for 24 h under dark conditions. Afterward, reaction products were magnetically collected and wash with DI water several times. The final product was re-dispersed in 5 mL of DI water.

3.4. Characterizations

Ultraviolet–visible–near infrared (UV-vis-NIR) diffuse reflectance spectra were employed to investigate the optical properties of different samples on a UV–3600i Plus UV-vis spectrometer. Fourier Transform Infrared (FT-IR) spectroscopy was used to determine the chemical structure of the samples with Thermo Fisher Nicolet iS50 in the range of 400 cm⁻¹ to 4000 cm⁻¹. Powder X-ray diffraction (PXRD) pattern from 10° to 80° was conducted to characterize the crystal structure of the as-prepared samples using Bruker AXS D8 Advance diffractometer with Cu K α radiation ($v = 2^\circ/\text{min}$, 40 kV, 40 mA). The morphology and microstructure of different samples were examined by scanning electron microscopy (SEM) on ZEISS Gemini 300 and transmission electron microscopy (TEM) on FEI TF20 Super-X. A vibrating sample magnetometer (VSM) from Quantum Design PPMS–9 was used to measure the magnetic properties of the synthesized nanocomposite. Zeta potential was measured using Nano-Brook Omni (Brookhaven Instruments, Billerica, MA, USA).

3.5. Peroxidase-Like Activity Characterization

The peroxidase-like activity of the Fe₃O₄@PEI@Ag structure was investigated by using TMB as chromogenic substrates in the presence of H₂O₂. The Fe₃O₄@PEI@Ag structure reacted with H₂O₂ to produce a sufficient amount of ·OH, which was able to oxidize TMB to TMBox blue product, as following Equation (8). We investigated the peroxidase activity by mixing different samples with TMB solution in DMSO and H₂O₂. Briefly, samples were prepared in the phosphate buffer (pH 5.8), followed by the addition of H₂O₂ and TMB solution. After 10 min, the absorbance change of 652 nm from the oxidation product of TMB was used to monitor all catalytic activities. The pH-dependent peroxidase-like activities were explored by adjusting the pH of phosphate buffer for 10 min before measurements. The relationship between catalytic effect and concentration was verified by varying only the concentration of Fe₃O₄@PEI@Ag.

In order to investigate the catalytic activity of the Fe₃O₄@PEI@Ag structure, a number of steady-state experiments were conducted by varying concentrations of either H₂O₂ or TMB while keeping the remaining parameters constant. The final catalyst concentration of Fe₃O₄@PEI@Ag for the kinetics study was 200 µg·mL⁻¹. The aqueous solutions of different samples, H₂O₂ solution, and TMB in DMSO were prepared, respectively. For the kinetics study, 100 µL of H₂O₂ was fully mixed with 700 µL of phosphate buffer (pH 5.8) and 100 µL of TMB. The additional 100 µL of samples were added to the above mixture to start the catalysis process. After sufficient mixing, UV-vis detection was performed to observe the absorption value of the reaction products at 652 nm. The kinetics were investigated using the below Michaelis–Menten Equation (8).

$$V_0 = V_{\max} \frac{[S]}{K_m + [S]} \quad (8)$$

where V_0 represents the initial velocity, V_{\max} refers to the maximum reaction velocity, and $[S]$ is the concentration of substrate.

3.6. Colorimetric Detection of Glucose and Cytotoxicity Measurement of Fe₃O₄@PEI@Ag and Fe₃O₄@PEI@Ag@ICG Structures

Colorimetric detection of glucose: In clinical diagnosis, the glucose level in urine or blood samples are important for assessing the health of patients. The Fe₃O₄@PEI@Ag was evaluated for their potential application as mimics of HRP in glucose detection. H₂O₂

is an intermediate product of the glucose oxidation reaction by the action of glucose oxidase. Glucose oxidase reacted with glucose to produce H_2O_2 , which reacted with $Fe_3O_4@PEI@Ag$ in redox reaction and the reaction products further combined with TMB to produce blue TMB_{ox}.

- (a) A total of 100 μ L of GOx and 100 μ L glucose with different concentrations in 300 μ L Phosphate-buffered Saline (pH 7.4) were incubated at 37 °C for 15 min;
- (b) A total of 300 μ L phosphate buffer (pH 5.8), 100 μ L TMB, 100 μ L $Fe_3O_4@PEI@Ag$ aqueous solutions were added to the above glucose reaction solution (0.5 mL);
- (c) The mixed solution was incubated at 37 °C for 15 min;
- (d) UV-vis detection was performed to observe the absorption value of the reaction products at 652 nm. In the control experiments, 10 mM lactose, 10 mM fructose, 10 mM maltose, and 10 mM Sucrose were used instead of glucose, respectively.

Cytotoxicity measurement: The cytotoxic effect of $Fe_3O_4@PEI@Ag$ and $Fe_3O_4@PEI@Ag@ICG$ structures on human keratinocytes cells (Hacat cells) was determined using the MTT assay. In addition, Hacat cells were obtained from the American Type Culture Collection (Rockville, MD, USA). The cells were stained in accordance with the manufacturer-recommended method and were measured using fluorescence signal analysis equipment. The chemicals used included Dulbecco's Modified Eagle Medium (DMEM), phosphate-buffered saline, 3-(4,5-dimethyl-2-thiazolyl)-2,5-diphenyl-2H-tetrazolium bromide (MTT, Sigma Aldrich, St. Louis, MI, USA), dimethyl sulfoxide (DMSO, Sigma Aldrich, St. Louis, MI, USA). Measurements were carried out on a multi-detection microplate Synergy HT reader (BioTek, Winooski, VT, USA). We used 96 well plates (Fisher Scientific, Shanghai, China) for cell line cultivation, a centrifugal machine (Eppendorf, Hamburg, Germany), and a glass coverslip (Shitai, Jiangsu, China).

The MTT assay was used to examine the cytotoxic effect and was carried out in six different groups. Briefly, Hacat cells were cultured for 12 h in a 96-well plate (1×10^4 cells per well) and treated with various agents ($Fe_3O_4@PEI@Ag$ and $Fe_3O_4@PEI@Ag@ICG$ composites) at gradient concentrations (0, 5, 25, 50, 100, and 200 μ g·mL⁻¹) at 37 °C and under 5% CO₂ atmosphere for 2 h. Next, the cells were cultured for another 2 h and subsequently treated with 20 μ L MTT solution (500 μ g·mL⁻¹ dissolved in PBS). After an additional 4 h incubation at 37 °C and under 5% of CO₂, the old medium was replaced with 200 μ L DMSO and gently agitated for 10 min. The experiment was performed in triplicate for each sample. Finally, the optical absorbance intensity at 490 nm and 630 nm in each well was measured using a microplate reader. The absorbance of each well was measured at 570 nm with an ELISA plate reader.

3.7. The Photothermal Effect Measurement under NIR-Light Activations

A NIR laser of 808 nm (LR-MFJ-808/2000 mW, LeiRui, Changchun, China) was used to activate the photothermal effects of the materials. A total of 200 μ L of $Fe_3O_4@PEI@Ag@ICG$ structure with gradient concentrations were loaded into each transparent Eppendorf (capacity: 1.5 mL) and exposed to NIR irradiation for 5 min. The laser spot was adjusted to cover the whole surface of the samples. The changes in temperature are recorded in real-time by an online thermometer. The photothermal images of different samples were shot every 20 s by an infrared imaging device (FOTRIC 360, Shanghai, China). In order to investigate photothermal stability, one cycle of NIR laser irradiation was applied to the $Fe_3O_4@PEI@Ag@ICG$ structure dispersion, and the resultant temperature variations were recorded in real-time during laser irradiation and cooling processes.

4. Conclusions

In summary, $Fe_3O_4@PEI@Ag$ structure was fabricated via a facile approach in water mediums, the resulting size of which was about 150 nm. The peroxidase-mimicking properties were further explored by TMB, which confirmed that the $Fe_3O_4@PEI@Ag$ structure possesses an enzymatic performance with high efficiency due to the synergistic interaction of each composite. Based on the chromogenic reaction of TMB- H_2O_2 and GOx, it

triggered the generation of H₂O₂ from glucose. The catalytic reaction of Fe₃O₄@PEI@Ag and colorimetric glucose assay were successfully constructed with excellent sensitivity and selectivity. It could be treated as a replaceable agent to detect glucose in real samples. By integrating it with an ICG photosensitizer, it enhanced the absorbance intensity but, also, Fe₃O₄@PEI@Ag@ICG gave red-shift in the NIR-I window. The photothermal property was achieved by irradiation at 808 nm, which showed the synergistic effect and excellent performance at high efficiency in temperature-controlled conditions. The Fe₃O₄@PEI@Ag@ICG structure has a faster photothermal response, which can rise to the temperature limit in 3.5 min and quickly decrease to RT within 10 min once the laser source is removed. It should be considered as a potential path for making complex composites, and the subsequent development could offer the possibility of applying this structure to photothermal therapies.

Supplementary Materials: The following supporting information can be downloaded at: <https://www.mdpi.com/article/10.3390/ijms231810743/s1>.

Author Contributions: Conceptualization, X.M.; methodology, T.W. and X.H. (Xi Hu); validation, T.W. and X.H. (Xi Hu); formal analysis, T.W. and X.H. (Xi Hu); investigation, T.W. and X.H. (Xi Hu); resources, C.H., Q.W. and Z.W.; data curation, C.H., Z.W., X.H. (Xiong He) and Y.Y.; writing—original draft preparation, T.W. and X.H. (Xi Hu); writing—review and editing, X.M., T.W. and X.H. (Xi Hu); visualization, T.W. and X.H. (Xi Hu); supervision, X.M.; project administration, X.M. All authors have read and agreed to the published version of the manuscript.

Funding: This work was supported by the Science and Technology Research program of Chongqing Municipal Education Commission (Grants no. KJQN201900436, KJQN202000420), the Science and Technology Planning Project of Yuzhong District, Chongqing, China (Grants no.: 20200118), the National Natural Science Foundation of China (Grants no.: 81501617).

Institutional Review Board Statement: Not applicable.

Informed Consent Statement: Not applicable.

Data Availability Statement: The data presented in this study are available on request from the corresponding author.

Conflicts of Interest: The authors declare no conflict of interest.

References

1. Liu, B.; Romine, A.M.; Rubel, C.Z.; Engle, K.M.; Shi, B.F. Transition-Metal-Catalyzed, Coordination-Assisted Functionalization of Nonactivated C(sp³)-H Bonds. *Chem. Rev.* **2021**, *121*, 14957–15074. [[CrossRef](#)]
2. Quintana, C.; Cifuentes, M.P.; Humphrey, M.G. Transition metal complex/gold nanoparticle hybrid materials. *Chem. Soc. Rev.* **2020**, *49*, 2316–2341. [[CrossRef](#)]
3. Zhang, X.P.; Chandra, A.; Lee, Y.M.; Cao, R.; Ray, K.; Nam, W. Transition metal-mediated O-O bond formation and activation in chemistry and biology. *Chem. Soc. Rev.* **2021**, *50*, 4804–4811. [[CrossRef](#)]
4. van de L'Isle, M.O.N.; Ortega-Liebana, M.C.; Unciti-Broceta, A. Transition metal catalysts for the bioorthogonal synthesis of bioactive agents. *Curr. Opin. Chem. Biol.* **2021**, *61*, 32–42. [[CrossRef](#)]
5. Klein, S.; Stiegler, L.M.S.; Harreiss, C.; Distel, L.V.R.; Neuhuber, W.; Spiecker, E.; Hirsch, A.; Kryschi, C. Understanding the Role of Surface Charge in Cellular Uptake and X-ray-Induced ROS Enhancing of Au-Fe₃O₄ Nanoheterodimers. *ACS Appl. Bio Mater.* **2018**, *1*, 2002–2011. [[CrossRef](#)]
6. Luo, Y.; Fu, Y.; Huang, Z.; Li, M. Transition metals and metal complexes in autophagy and diseases. *J. Cell Physiol.* **2021**, *236*, 7144–7158. [[CrossRef](#)]
7. Gao, L.; Zhuang, J.; Nie, L.; Zhang, J.; Zhang, Y.; Gu, N.; Wang, T.; Feng, J.; Yang, D.; Perrett, S.; et al. Intrinsic peroxidase-like activity of ferromagnetic nanoparticles. *Nat. Nanotechnol.* **2007**, *2*, 577–583. [[CrossRef](#)]
8. Liu, W.; Guo, J.; Chen, C.; Ni, P.; Jiang, Y.; Zhang, C.; Wang, B.; Lu, Y. Ultrathin PdCu alloy nanosheet-assembled 3D nanoflowers with high peroxidase-like activity toward colorimetric glucose detection. *Mikrochim. Acta* **2021**, *188*, 114. [[CrossRef](#)]
9. Wei, H.; Wang, E. Nanomaterials with enzyme-like characteristics (nanozymes): Next-generation artificial enzymes. *Chem. Soc. Rev.* **2013**, *42*, 6060–6093. [[CrossRef](#)]
10. Chen, Z.W.; Yin, J.J.; Zhou, Y.T.; Zhang, Y.; Song, L.; Song, M.J.; Hu, S.L.; Gu, N. Dual Enzyme-like Activities of Iron Oxide Nanoparticles and Their Implication for Diminishing Cytotoxicity. *ACS Nano* **2012**, *6*, 4001–4012. [[CrossRef](#)]

11. Kang, X.; Sun, T.; Zhang, L.; Zhou, C.; Xu, Z.; Du, M.; Xiao, S.; Liu, Y.; Gong, M.; Zhang, D. Synergistic Theranostics of Magnetic Resonance Imaging and Photothermal Therapy of Breast Cancer Based on the Janus Nanostructures Fe₃O₄-Aushell-PEG. *Int. J. Nanomed.* **2021**, *16*, 6383–6394. [[CrossRef](#)]
12. Dutta, B.; Nema, A.; Shetake, N.G.; Gupta, J.; Barick, K.C.; Lawande, M.A.; Pandey, B.N.; Priyadarsini, I.K.; Hassan, P.A. Glutamic acid-coated Fe₃O₄ nanoparticles for tumor-targeted imaging and therapeutics. *Mater. Sci. Eng. C Mater. Biol. Appl.* **2020**, *112*, 110915. [[CrossRef](#)]
13. Rajkumar, S.; Prabaharan, M. Multi-functional core-shell Fe₃O₄@Au nanoparticles for cancer diagnosis and therapy. *Colloids Surf. B Biointerfaces* **2019**, *174*, 252–259.
14. Klein, S.; Harreiss, C.; Menter, C.; Hummer, J.; Distel, L.V.R.; Meyer, K.; Hock, R.; Kryschi, C. NOBF₄-Functionalized Au-Fe₃O₄ Nanoheterodimers for Radiation Therapy: Synergy Effect Due to Simultaneous Reactive Oxygen and Nitrogen Species Formation. *ACS Appl. Mater. Inter.* **2018**, *10*, 17071–17080. [[CrossRef](#)]
15. Li, J.; Xu, Q.; Wei, X.; Hao, Z. Electrogenerated chemiluminescence immunosensor for *Bacillus thuringiensis* Cry1Ac based on Fe₃O₄@Au nanoparticles. *J. Agric. Food Chem.* **2013**, *61*, 1435–1440. [[CrossRef](#)]
16. Zhang, P.; Zhao, Q.; Shi, M.; Yin, C.; Zhao, Z.; Shen, K.; Qiu, Y.; Xiao, Y.; Zhao, Y.; Yang, X.; et al. Fe₃O₄@TiO₂-Laden Neutrophils Activate Innate Immunity via Photosensitive Reactive Oxygen Species Release. *Nano Lett.* **2020**, *20*, 261–271. [[CrossRef](#)]
17. Nosrati, H.; Baghdadchi, Y.; Abbasi, R.; Barsbay, M.; Ghaffarlou, M.; Abhari, F.; Mohammadi, A.; Kavetsky, T.; Bochani, S.; Rezaeejam, H.; et al. Iron oxide and gold bimetallic radiosensitizers for synchronous tumor chemoradiation therapy in 4T1 breast cancer murine model. *J. Mater. Chem. B* **2021**, *9*, 4510–4522. [[CrossRef](#)]
18. Tian, L.; Wang, X.J.; Qi, J.X.; Yao, Q.; Oderinde, O.; Yao, C.; Song, W.; Shu, W.X.; Chen, P.; Wang, Y.H. Improvement of the surface wettability of silicone hydrogel films by self-assembled hydroxypropyltrimethyl ammonium chloride chitosan mixed colloids. *Coll. Surf. A* **2018**, *558*, 422–428. [[CrossRef](#)]
19. He, H.; Sun, D.W.; Pu, H.; Huang, L. Bridging Fe₃O₄@Au nanoflowers and Au@Ag nanospheres with aptamer for ultrasensitive SERS detection of aflatoxin B1. *Food Chem.* **2020**, *324*, 126832. [[CrossRef](#)]
20. Nguyen, T.T.; Mammeri, F.; Ammar, S.; Nguyen, T.B.N.; Nguyen, T.N.; Nghiem, T.H.L.; Thuy, N.T.; Ho, T.A. Preparation of Fe₃O₄-Ag Nanocomposites with Silver Petals for SERS Application. *Nanomaterials* **2021**, *11*, 1288. [[CrossRef](#)]
21. Karami, B.; Hoseini, S.J.; Eskandari, K.; Ghasemi, A.; Nasrabadi, H. Synthesis of xanthene derivatives by employing Fe₃O₄ nanoparticles as an effective and magnetically recoverable catalyst in water. *Catal. Sci. Technol.* **2012**, *2*, 331–338. [[CrossRef](#)]
22. Chen, R.; Sun, Y.; Huo, B.; Mao, Z.; Wang, X.; Li, S.; Lu, R.; Li, S.; Liang, J.; Gao, Z. Development of Fe₃O₄@Au nanoparticles coupled to Au@Ag core-shell nanoparticles for the sensitive detection of zearalenone. *Anal. Chim. Acta* **2021**, *1180*, 338888. [[CrossRef](#)]
23. Wang, C.W.; Gu, B.; Liu, Q.Q.; Pang, Y.F.; Xiao, R.; Wang, S.Q. Combined use of vancomycin-modified Ag-coated magnetic nanoparticles and secondary enhanced nanoparticles for rapid surface-enhanced Raman scattering detection of bacteria. *Int. J. Nanomed.* **2018**, *13*, 1159–1178. [[CrossRef](#)]
24. Ye, Y.; Mao, S.; He, S.; Xu, X.; Cao, X.; Wei, Z.; Gunasekaran, S. Ultrasensitive electrochemical genosensor for detection of CaMV35S gene with Fe₃O₄-Au@Ag nanoprobe. *Talanta* **2020**, *206*, 120205. [[CrossRef](#)]
25. Najafipour, A.; Ghariéh, A.; Fassihi, A.; Sadeghi-Aliabadi, H.; Mahdavian, A.R. MTX-Loaded Dual Thermoresponsive and pH-Responsive Magnetic Hydrogel Nanocomposite Particles for Combined Controlled Drug Delivery and Hyperthermia Therapy of Cancer. *Mol. Pharm.* **2021**, *18*, 275–284. [[CrossRef](#)]
26. Xu, C.; Wang, B.; Sun, S. Dumbbell-like Au-Fe₃O₄ nanoparticles for target-specific platinum delivery. *J. Am. Chem. Soc.* **2009**, *131*, 4216–4217. [[CrossRef](#)]
27. Wang, X.; Cao, W.; Qin, L.; Lin, T.; Chen, W.; Lin, S.; Yao, J.; Zhao, X.; Zhou, M.; Hang, C.; et al. Boosting the Peroxidase-Like Activity of Nanostructured Nickel by Inducing Its 3+ Oxidation State in LaNiO₃ Perovskite and Its Application for Biomedical Assays. *Theranostics* **2017**, *7*, 2277–2286. [[CrossRef](#)]
28. Wang, Z.; Yang, X.; Yang, J.; Jiang, Y.; He, N. Peroxidase-like activity of mesoporous silica encapsulated Pt nanoparticle and its application in colorimetric immunoassay. *Anal. Chim. Acta* **2015**, *862*, 53–63. [[CrossRef](#)]
29. Shi, W.J.; Fan, H.; Ai, S.Y.; Zhu, L.S. Honeycomb-like nitrogen-doped porous carbon supporting Pt nanoparticles as enzyme mimic for colorimetric detection of cholesterol. *Sens. Actuat. B-Chem.* **2015**, *221*, 1515–1522. [[CrossRef](#)]
30. Zhou, N.A.; Zou, S.Y.; Zou, L.; Shen, R.D.; Zhou, Y.M.; Ling, L.S. Peroxidase-like activity of palladium nanoparticles on hydrogen-bond supramolecular structures over a broader pH range and their application in glucose sensing. *Can. J. Chem.* **2019**, *97*, 317–323. [[CrossRef](#)]
31. Wang, C.; Daimon, H.; Sun, S.H. Dumbbell-like Pt-Fe₃O₄ Nanoparticles and Their Enhanced Catalysis for Oxygen Reduction Reaction. *Nano Lett.* **2009**, *9*, 1493–1496. [[CrossRef](#)]
32. Wei, F.; Cui, X.Y.; Wang, Z.; Dong, C.C.; Li, J.D.; Han, X.J. Recoverable peroxidase-like Fe₃O₄@MoS₂-Ag nanozyme with enhanced antibacterial ability. *Chem. Eng. J.* **2021**, *408*, 127240. [[CrossRef](#)]
33. Pan, L.; Zhu, Q.Y.; Li, L. Synthesis and electrocatalytic properties of Ag_xAu_y/Fe₃O₄ composite microspheres and nanoparticles. *J. Iran. Chem. Soc.* **2021**, *18*, 1211–1217. [[CrossRef](#)]
34. Li, Y.Y.; Li, Q.; Fu, Y.; Hao, M.Z.; Wang, W.C.; Zou, H.; Zhang, L.Q.; Tian, M. A Novel Method for the Preparation of Conductive and Magnetic Fe₃O₄@Ag Hybrid Nanoparticles. *J. Nanosci. Nanotechnol.* **2016**, *16*, 8431–8438. [[CrossRef](#)]

35. Jiang, H.; Chen, Z.; Cao, H.; Huang, Y. Peroxidase-like activity of chitosan stabilized silver nanoparticles for visual and colorimetric detection of glucose. *Analyst* **2012**, *137*, 5560–5564. [[CrossRef](#)]
36. Baghayeri, M.; Veisi, H. Fabrication of a facile electrochemical biosensor for hydrogen peroxide using efficient catalysis of hemoglobin on the porous Pd@Fe₃O₄-MWCNT nanocomposite. *Biosens. Bioelectron.* **2015**, *74*, 190–198. [[CrossRef](#)]
37. Zheng, C.; Ke, W.J.; Yin, T.X.; An, X.Q. Intrinsic peroxidase-like activity and the catalytic mechanism of gold@carbon dots nanocomposites. *RSC Adv.* **2016**, *6*, 35280–35286. [[CrossRef](#)]
38. Ke, F.; Wang, L.; Zhu, J. Multifunctional Au-Fe₃O₄@MOF core-shell nanocomposite catalysts with controllable reactivity and magnetic recyclability. *Nanoscale* **2015**, *7*, 1201–1208. [[CrossRef](#)]
39. Chudasama, B.; Vala, A.K.; Andhariya, N.; Upadhyay, R.V.; Mehta, R.V. Enhanced Antibacterial Activity of Bifunctional Fe₃O₄-Ag Core-Shell Nanostructures. *Nano Res.* **2009**, *2*, 955–965. [[CrossRef](#)]
40. Yong, C.Y.; Chen, X.Q.; Xiang, Q.; Li, Q.; Xing, X.D. Recyclable magnetite-silver heterodimer nanocomposites with durable antibacterial performance. *Bioact. Mater.* **2018**, *3*, 80–86. [[CrossRef](#)]
41. Xue, P.; Yang, R.; Sun, L.; Li, Q.; Zhang, L.; Xu, Z.; Kang, Y. Indocyanine Green-Conjugated Magnetic Prussian Blue Nanoparticles for Synchronous Photothermal/Photodynamic Tumor Therapy. *Nano-Micro Lett.* **2018**, *10*, 74. [[CrossRef](#)]
42. Yang, J.H.; Zou, P.; Yang, L.L.; Cao, J.; Sun, Y.F.; Han, D.L.; Yang, S.; Wang, Z.; Chen, G.; Wang, B.; et al. A comprehensive study on the synthesis and paramagnetic properties of PEG-coated Fe₃O₄ nanoparticles. *Appl. Surf. Sci.* **2014**, *303*, 425–432. [[CrossRef](#)]
43. Leng, W.N.; Pati, P.; Vikesland, P.J. Room temperature seed mediated growth of gold nanoparticles: Mechanistic investigations and life cycle assesment. *Environ. Sci. Nano* **2015**, *2*, 440–453. [[CrossRef](#)]
44. Wang, L.; Sun, Y.; Wang, J.; Wang, J.; Yu, A.; Zhang, H.; Song, D. Preparation of surface plasmon resonance biosensor based on magnetic core/shell Fe₃O₄/SiO₂ and Fe₃O₄/Ag/SiO₂ nanoparticles. *Colloids Surf. B Biointerfaces* **2011**, *84*, 484–490. [[CrossRef](#)]
45. Zhang, J.L.; Srivastava, R.S.; Misra, R.D. Core-shell magnetite nanoparticles surface encapsulated with smart stimuli-responsive polymer: Synthesis, characterization, and LCST of viable drug-targeting delivery system. *Langmuir* **2007**, *23*, 6342–6351. [[CrossRef](#)]
46. Gao, W.; Li, L.; Zhang, X.; Luo, L.; He, Y.; Cong, C.; Gao, D. Nanomagnetic liposome-encapsulated parthenolide and indocyanine green for targeting and chemo-photothermal antitumor therapy. *Nanomedicine* **2020**, *15*, 871–890. [[CrossRef](#)]
47. Jomma, E.Y.; Ding, S.N. One-Pot Hydrothermal Synthesis of Magnetite Prussian Blue Nano-Composites and Their Application to Fabricate Glucose Biosensor. *Sensors* **2016**, *16*, 243.
48. Wang, S.J.; Chen, C.S.; Chen, L.C. Prussian blue nanoparticles as nanocargoes for delivering DNA drugs to cancer cells. *Sci. Technol. Adv. Mat.* **2013**, *14*, 044405. [[CrossRef](#)]
49. Li, T.T.; Geng, Y.; Zhang, H.X.; Wang, J.; Feng, Y.; Chen, Z.Y.; Xie, X.X.; Qin, X.; Li, S.; Wu, C.H.; et al. A versatile nanoplatform for synergistic chemo-photothermal therapy and multimodal imaging against breast cancer. *Expert Opin. Drug Deliv.* **2020**, *17*, 725–733.
50. Xu, Y.; Jian, G.; Peng, Y.; Liu, Z.; Hu, X. Lubricating mechanism of Fe₃O₄@MoS₂ core-shell nanocomposites as oil additives for steel/steel contact. *Tribol. Int.* **2018**, *121*, 241–251. [[CrossRef](#)]
51. Liu, Y.; Yuan, M.; Qiao, L.; Guo, R. An efficient colorimetric biosensor for glucose based on peroxidase-like protein-Fe₃O₄ and glucose oxidase nanocomposites. *Biosens. Bioelectron.* **2014**, *52*, 391–396. [[CrossRef](#)]
52. Meng, X.Q.; Li, D.D.; Chen, L.; He, H.L.; Wang, Q.; Hong, C.Y.; He, J.Y.; Gao, X.F.; Yang, Y.L.; Jiang, B.; et al. High-Performance Self-Cascade Pyrite Nanozymes for Apoptosis-Ferroptosis Synergistic Tumor Therapy. *ACS Nano* **2021**, *15*, 5735–5751.
53. Ma, L.; Zhu, J.; Wu, C.; Li, D.; Tang, X.H.; Zhang, Y.; An, C.H. Three-dimensional MoS₂ nanoflowers supported Prussian blue and Au nanoparticles: A peroxidase-mimicking catalyst for the colorimetric detection of hydrogen peroxide and glucose. *Spectrochim. Acta A* **2021**, *259*, 119886. [[CrossRef](#)]
54. An, Q.; Sun, C.; Li, D.; Xu, K.; Guo, J.; Wang, C. Peroxidase-like activity of Fe₃O₄@carbon nanoparticles enhances ascorbic acid-induced oxidative stress and selective damage to PC-3 prostate cancer cells. *ACS Appl. Mater. Interfaces* **2013**, *5*, 13248–13257.
55. Su, L.; Feng, J.; Zhou, X.M.; Ren, C.L.; Li, H.H.; Chen, X.G. Colorimetric Detection of Urine Glucose Based ZnFe₂O₄ Magnetic Nanoparticles. *Anal. Chem.* **2012**, *84*, 5753–5758. [[CrossRef](#)]
56. Huang, W.; Lin, T.Y.; Cao, Y.; Lai, X.Y.; Peng, J.; Tu, J.C. Hierarchical NiCo₂O₄ Hollow Sphere as a Peroxidase Mimetic for Colorimetric Detection of H₂O₂ and Glucose. *Sensors* **2017**, *17*, 217.
57. Chen, J.; Shu, Y.; Li, H.; Xu, Q.; Hu, X. Nickel metal-organic framework 2D nanosheets with enhanced peroxidase nanozyme activity for colorimetric detection of H₂O₂. *Talanta* **2018**, *189*, 254–261. [[CrossRef](#)]
58. Tan, H.; Li, Q.; Zhou, Z.; Ma, C.; Song, Y.; Xu, F.; Wang, L. A sensitive fluorescent assay for thiamine based on metal-organic frameworks with intrinsic peroxidase-like activity. *Anal Chim Acta* **2015**, *856*, 90–95.
59. Li, S.L.; Li, H.; Chen, F.J.; Liu, J.; Zhang, H.L.; Yang, Z.Y.; Wang, B.D. Strong coupled palladium nanoparticles decorated on magnetic graphene nanosheets as enhanced peroxidase mimetics for colorimetric detection of H₂O₂. *Dyes Pigment.* **2016**, *125*, 64–71. [[CrossRef](#)]
60. Kuo, C.H.; Lamontagne, L.K.; Brodsky, C.N.; Chou, L.Y.; Zhuang, J.; Sneed, B.T.; Sheehan, M.K.; Tsung, C.K. The effect of lattice strain on the catalytic properties of Pd nanocrystals. *ChemSusChem* **2013**, *6*, 1993–2000. [[CrossRef](#)]
61. Song, Y.J.; Qu, K.G.; Zhao, C.; Ren, J.S.; Qu, X.G. Graphene Oxide: Intrinsic Peroxidase Catalytic Activity and Its Application to Glucose Detection. *Adv. Mater.* **2010**, *22*, 2206–2210. [[CrossRef](#)] [[PubMed](#)]
62. Ding, Y.N.; Yang, B.C.; Liu, H.; Liu, Z.X.; Zhang, X.; Zheng, X.W.; Liu, Q.Y. FePt-Au ternary metallic nanoparticles with the enhanced peroxidase-like activity for ultrafast colorimetric detection of H₂O₂. *Sens. Actuat. B-Chem.* **2018**, *259*, 775–783. [[CrossRef](#)]

63. Mvango, S.; Mashazi, P. Synthesis, characterization of copper oxide-gold nanoalloys and their peroxidase-like activity towards colorimetric detection of hydrogen peroxide and glucose. *Mat. Sci. Eng. C-Mater.* **2019**, *96*, 814–823. [[CrossRef](#)] [[PubMed](#)]
64. Singh, S.; Mitra, K.; Singh, R.; Kumari, A.; Sen Gupta, S.K.; Misra, N.; Maiti, P.; Ray, B. Colorimetric detection of hydrogen peroxide and glucose using brominated graphene. *Anal. Methods* **2017**, *9*, 6675–6681. [[CrossRef](#)]
65. Ortiz-Gomez, I.; Salinas-Castillo, A.; Garcia, A.G.; Alvarez-Bermejo, J.A.; de Orbe-Paya, I.; Rodriguez-Dieguez, A.; Capitan-Vallvey, L.F. Microfluidic paper-based device for colorimetric determination of glucose based on a metal-organic framework acting as peroxidase mimetic. *Microchim. Acta* **2018**, *185*, 47. [[CrossRef](#)]
66. Choleva, T.G.; Gatselou, V.A.; Tsogas, G.Z.; Giokas, D.L. Intrinsic peroxidase-like activity of rhodium nanoparticles, and their application to the colorimetric determination of hydrogen peroxide and glucose. *Microchim. Acta* **2018**, *185*, 22. [[CrossRef](#)]
67. Wang, X.; Li, F.; Cai, Z.Q.; Liu, K.F.; Li, J.; Zhang, B.Y.; He, J.B. Sensitive colorimetric assay for uric acid and glucose detection based on multilayer-modified paper with smartphone as signal readout. *Anal. Bioanal. Chem.* **2018**, *410*, 2647–2655. [[CrossRef](#)]
68. Sun, J.; Li, C.; Qi, Y.; Guo, S.; Xue, L. Optimizing Colorimetric Assay Based on V₂O₅ Nanozymes for Sensitive Detection of H₂O₂ and Glucose. *Sensors* **2016**, *16*, 584. [[CrossRef](#)]
69. Mahmoudi, M.; Simchi, A.; Milani, A.S.; Stroeve, P. Cell toxicity of superparamagnetic iron oxide nanoparticles. *J. Colloid Interface Sci.* **2009**, *336*, 510–518. [[CrossRef](#)]
70. Holzer, W.; Mauerer, M.; Penzkofer, A.; Szeimies, R.M.; Abels, C.; Landthaler, M.; Baumler, W. Photostability and thermal stability of indocyanine green. *J. Photochem. Photobiol. B* **1998**, *47*, 155–164. [[CrossRef](#)]
71. Wang, S.; Riedinger, A.; Li, H.; Fu, C.; Liu, H.; Li, L.; Liu, T.; Tan, L.; Barthel, M.J.; Pugliese, G.; et al. Plasmonic copper sulfide nanocrystals exhibiting near-infrared photothermal and photodynamic therapeutic effects. *ACS Nano* **2015**, *9*, 1788–1800. [[CrossRef](#)] [[PubMed](#)]
72. Xue, P.; Hou, M.; Sun, L.; Li, Q.; Zhang, L.; Xu, Z.; Kang, Y. Calcium-carbonate packaging magnetic polydopamine nanoparticles loaded with indocyanine green for near-infrared induced photothermal/photodynamic therapy. *Acta Biomater.* **2018**, *81*, 242–255. [[CrossRef](#)] [[PubMed](#)]